NeuroImage: Clinical 24 (2019) 102101

Contents lists available at ScienceDirect

NeuroImage: Clinical

journal homepage: www.elsevier.com/locate/ynicl

Severe asymptomatic carotid stenosis is associated with robust reductions in homotopic functional connectivity

Gao Lei[a,1], Wang Tao[b,c,1], Qian Tianyi[d], Xiao Feng[a], Bai Lijun[e], Junjian Zhang[c,*], Xu Haibo[a,*]

[a] Department of Radiology, Zhongnan Hospital of Wuhan University, Wuchang District, Wuhan City, Hubei Province 430071, China
[b] Department of Neurology, the First College of Clinical Medical Science, China Three Gorges University, Yichang, China
[c] Department of Neurology, Zhongnan Hospital of Wuhan University, Wuchang District, Wuhan City, Hubei Province 430071, China
[d] MR Collaboration, Siemens Healthcare China, Beijing, China
[e] The Key Laboratory of Biomedical Information Engineering, Ministry of Education, Department of Biomedical Engineering, School of Life Science and Technology, Xi'an Jiaotong University, Xi'an 710049, China

ARTICLE INFO

Keywords:
Arterial spin labeling (ASL)
Susceptibility weighted imaging (SWI)
White matter hyperintensity (WMH)
Interhemispheric connectivity
Machine learning
Stroke

ABSTRACT

Severe (>70% narrowing) asymptomatic carotid stenosis (SACS) is associated with cognitive impairment and future strokes, and connectivity basis for the remote brain consequences is poorly understood. Here we explored homotopic connectivity and parenchymal lesions measured by multimodal magnetic resonance imaging (MRI) parameters in patients with SACS. Twenty-four patients with SACS (19 males/5 females; 64.25 ± 7.18 years), 24 comorbidities-matched controls (19 males/5 females; 67.16 ± 6.10 years), and an independent sample of elderly healthy controls (39 females/45 males; 57.92 ± 4.94 years) were included. Homotopic functional connectivity (FC) of resting-state functional MRI and structural connectivity (SC) of deterministic tractography were assessed. Arterial spin labeling based cerebral perfusion, susceptibility weighted imaging based microhemorrhagic lesions, and T2-weighted white matter hyperintensities were also quantified. Significant and robust homotopic reductions (validated by the independent dataset and support vector machine-based machine learning) were identified in the Perisylvian fissure in patients with SACS (false discovery rate corrected, voxel $p < 0.05$). These involved regions span across several large-scale brain systems, which include the somatomotor, salience, dorsal attention, and orbitofrontal-limbic networks. This significantly reduced homotopic FC can be partially explained by the corrected white matter hyperintensity size. Further association analyses suggest that the decreased homotopic FC in these brain regions is most closely associated with delayed memory recall, sensorimotor processing, and other simple cognitive functions. Together, these results suggest that SACS predominately affects the lower-order brain systems, while higher-order systems, especially the topographies of default mode network, are least impacted initially, but may serve as a hallmark precursor to vascular dementia. Thus, assessment of homotopic FC may provide a means of noninvasively tracking the progression of downstream brain damage following asymptomatic carotid stenosis.

1. Introduction

Patients with severe (> 70% narrowing) asymptomatic carotid stenosis (SACS) are at moderate to high risk of progressive cognitive deterioration and cerebrovascular events (de Weerd et al., 2014). Therefore, the clinical focus for these patients is the management of future strokes. However, best management practices, and which populations might benefit from interventions, are still debated (Rosenfield et al., 2016). One reason for this lack of consensus stems from the poorly understood neural basis of SACS.

Compromised hemodynamics and connectivity may promote the etiology of cognitive decline and vulnerability to strokes. Pathologically, severe stenosis is associated with potential hemodynamic changes, silent cerebrovascular disease, and varying degrees of structural damage (van Veluw et al., 2017). Functionally, patients with SACS have reported altered connectivity that involves intra- and interhemispheric large-scale systems (Avelar et al., 2016; Baradaran et al., 2016; Cheng et al., 2012; Lin et al., 2014; Panczykowski et al., 2014).

Despite existing documentation, there is still a lack of objective imaging metric that may be noninvasively utilized to understand and

* Corresponding authors.
E-mail addresses: wdsjkx@163.com (J. Zhang), xuhaibo1120@hotmail.com (H. Xu).
[1] These authors contributed equally to this paper.

https://doi.org/10.1016/j.nicl.2019.102101
Received 29 April 2018; Received in revised form 5 October 2019; Accepted 18 November 2019
Available online 20 November 2019

track the progress of the disease. It is known that the most critical endpoint of SACS is the occurrence of ischemic strokes and vascular dementia. Both SACS and ischemic strokes preferentially affect low-level brain functions that are closely related to sensorimotor processing, and patients with SACS show similar declines in the same cognitive domains to those with strokes (Grefkes and Fink, 2014). Moreover, as a type of silent cerebrovascular disease, SACS can be considered a precursor to strokes. For example, patients with SACS show altered functional as well as structural connectivity that mimics ischemic stroke (Cheng et al., 2012; Lin et al., 2014; Panczykowski et al., 2014). Therefore, imaging measures that best capture stroke pathophysiology may also be beneficial for investigating SACS.

Considering the complexity and heterogeneous nature of carotid stenosis, metrics used for tracking the brain state should reflect multiple dimensions, such as cognition and disease sensitivity. Since the pioneering work of Biswal and colleagues (Biswal et al., 1995), resting-state functional magnetic resonance imaging (R-fMRI) has promoted the use of noninvasive assessments of the brain's functional architecture into clinical experimentation. Functional connectivity (FC) of R-fMRI measures hemodynamic correlations between regional low frequency (<0.1 Hz) blood oxygen level dependent (BOLD) signals. One architectural feature, functional homotopy, or voxel-mirrored homotopic interhemispheric connectivity (VMHC) (Zuo et al., 2010), quantifies voxel-wise functional connectivity of the mirror-symmetrical pairs of voxels between hemispheres. VMHC represents a robust metric (Zuo et al., 2013; Zuo and Xing, 2014) that reflects interhemispheric integration, which has been linked to stroke recovery (Grefkes and Fink, 2014; Siegel et al., 2016; van Meer et al., 2010) and other neurological and psychiatric disorders (Anderson et al., 2011; Hoptman et al., 2012).

In this study, we aimed to explore the homotopic FC changes of R-fMRI in patients with SACS, while considering: homotopic structural connectivity (SC) with deterministic tractography, white matter hyperintensity (WMH) loads with T2-weighted Fluid-attenuated inversion recovery (FLAIR), cerebral microbleeds with susceptibility weighted imaging (SWI), and cerebral blood flow (CBF) measured by pulsed arterial spin labeled (PASL). We hypothesized that patients with SACS would demonstrate significant and classifiable reduced functional homotopy, predominately in the somatomotor, attention, and executive systems, and the cerebral perfusion and silent lesions can partially explain these changes.

2. Methods

2.1. Participants

Twenty-four SACS patients were recruited between January 2015 and June 2016. The inclusion criteria were (a) 55 – 80 years; (b) unilateral internal carotid artery (ICA) stenosis ⩾70%; (c) right-handed; (d) free of stroke, transient ischemic attack, or dementia; (e) Modified Rankin Scale (Sulter et al., 1999) score of 0 or 1. Exclusion criteria were (a) contralateral ICA stenosis ⩾ 50%; (b) posterior circulation diseases; (c) Mini-Mental State Examination (MMSE) (Folstein et al., 1975) score < 26; (d) functional disability (Modified Rankin Scale ≥ 2); (e) severe systemic diseases and neuropsychiatric diseases; (f) contraindications for MRI; and (g) poorly educated (< 6 years). In this same timeframe, we recruited 24 comorbidities- and demographically- matched healthy controls (HCs). Additionally, we included an independent dataset of elderly HCs (age, 57.92 ± 4.94 years; 39 females/ 45 males) to validate our results. The present study was approved through the Medical Ethics Committee of the Affiliated Hospital of Zhongnan Hospital of Wuhan University, and all participants gave written informed consent. Detailed demographics and clinical measures are listed in Table. 1.

Table 1
Demographics and clinical characteristics.

	Healthy (n = 24)	Patients (n = 19)	p
Gender (Male/Female)	19/5	15/4	0.99[a]
Age (yrs.)	67.16 ± 6.10	64.25 ± 7.18	0.17
Education (yrs.)	11.13 ± 3.46	9.58 ± 2.83	0.12
Hypertension	18/6	17/2	0.23
Diabetes	4/20	4/15	0.71
Hyperlipidemia	11/13	9/10	0.92
Smoke	6/18	9/10	0.13
Affected side	–	7L/12R	–
MMSE	27.38 ± 0.65	26.84 ± 0.69	0.015*
MoCA	24.21 ± 1.56	23.26 ± 1.15	0.017*
Word fluency	37.13 ± 4.01	33.42 ± 6.20	0.258
Digit symbol substitution	31.50 ± 5.51	28.00 ± 4.74	0.029*
Backwards digit-span	6.46 ± 0.93	5.79 ± 0.98	0.042*
Forwards digit-span	4.46 ± 0.78	3.84 ± 0.83	0.021*
Immediate recall	35.79 ± 5.63	31.00 ± 4.45	0.004**
Delayed recall	6.50 ± 1.14	4.63 ± 1.57	<0.001***
WMHcorrected	−0.59 ± 1.01	0.64 ± 0.71	<0.001***
WMHsize (ml)	1.56 ± 3.05	10.76 ± 13.48	0.005**
WMHnumber	5.87 ± 6.31	13.42 ± 5.84	<0.001***

Data are presented as mean ± SD. Abbreviations: MMSE, Mini-Mental State Examination; MoCA, Montreal Cognitive Assessment; a, p-value was obtained using the two-tailed Chi-squared test; WMH = white matter hyperintensity; WMHcorrected, white matter hyperintensity (corrected by total cranial volume, and log10 transformed); WMHsize, white matter hyperintensity volumes; WMHnumber, number of WMH.

2.2. Neurobehavioral assessments

Neurobehavioral assessments, including the MMSE, the Montreal Cognitive Assessment (MoCA) (Nasreddine et al., 2005) Beijing Version, the Digit Symbol, and the Rey Auditory Verbal Learning Tests, were performed within seven days of MRI scan. The MMSE and MoCA Beijing Version were utilized to assess global cognition. The Digit Symbol Test required subjects to translate numbers to paired symbols as quickly as possible, and number of correct translations within 90 s was recorded. The Rey Auditory Verbal Learning Test (RAVLT) was used to evaluate memory and verbal learning ability. Participants were given a list of 15 unrelated words and asked to recall as many words as he/she could remember. This procedure was then repeated four more times. After a thirty-minute delay, the participants were once more asked to recall as many word as possible from the original list. The total number of the words immediately recalled during the first five repeats and the sum of the delayed recall were recorded. In the Verbal Memory Test, participants were required to repeat orally presented lists of numbers, beginning with a 2-number sequence, and increasing by one additional number for each correct performance. In the forward span, participants were asked to recite the span in forward order. In the backward span, participants were asked to recite the span in reverse order.

2.3. MRI data acquisition

MRI data were collected using a MAGNETOM Trio 3.0 T MR scanner (Siemens, Germany). The scanning sessions included (1) T1 high-resolution anatomical images (176 sagittal slices, 1-mm in-plane resolution); (2) resting-state BOLD volumes (33 axial slices, 3.8-mm slice thickness with a 0.3-mm gap, repetition time (TR) = 2 s, 240 volumes); (3) diffusion tensor imaging (DTI) (TR/ echo time (TE) = 6000/93 ms, matrix = 128 × 128, 44 axial slices, 2.0 mm slice thickness, b values =0 and 1000s/mm^2) in 64 directions; (4) susceptibility-weighted imaging (SWI) (TR/TE = 29/20 ms, voxel size 0.5 × 0.5 × 2 mm, 128 slices, 2 mm thickness); (5) fluid attenuated inversion recovery (FLAIR) sequence (TR/TE/ inversion time (TI) = 6000/396/2200 ms, voxel size 0.5 × 0.5 × 1 mm, 160 slices, 1 mm thickness); and (6) perfusion imaging using Q2TIPS pulsed arterial spin labeling (PASL) sequence (TR /TE = 2500/11 ms, matrix = 64 × 64, flip angle = 90°,

slice thickness = 6 mm). During the R-fMRI scan, subjects were asked to remain as till as possible, keep their eyes closed, not fall asleep, and avoid thinking systematically.

2.4. MRI data processing

2.4.1. Preprocessing of R-fMRI data

R-fMRI data were preprocessed using the Data Processing & Analysis for Brain Image (DPABI, rfmri.org/dpabi) (Yan et al., 2016), Statistical Parametric Mapping (SPM12, http://www.fil.ion.ucl.ac.uk), and MATLAB 2013a (https://www.mathworks.com), following conventional methods as previously described (Li et al., 2017). Briefly, these included (1) removal of the first 10 functional volumes, (2) slice timing correction, (3) realignment and correction for small head movements, (4) co-registration between individual T1 anatomical and the realigned functional volumes, (5) normalization into Montreal Neurological Institute (MNI152) space through Diffeomorphic Anatomical Registration Through Exponentiated Lie Algebra (DARTEL) (Ashburner, 2007), using an elderly sample representative template (60–70 years), (6) spatial smoothing with 6 mm full width half maximum (FWHM) Gaussian blur, (7) reduction of confounding factors via linear regression, including the signals from the white matter and cerebrospinal fluid, and linear and quadratic trends, (8) temporal filtering (0.01–0.1 Hz) of the time series, and finally (9) motion scrubbing (Power et al., 2012; Yan et al., 2013, 2016a) with a frame-wise displacement (FD) threshold of 0.5.

2.4.2. Quality assurance

To correct for head motion, we calculated the FD and took the following measures to reduce motion effects: (i) ensure that no subject was found with maximum displacement in one or more of the orthogonal directions > 0.5 mm or a maximum rotation > 0.5°; (ii) the voxel-specific FD (FDvox) described as Yan et al. (2013) was calculated for each subject, and considered as nuisance covariate in the statistical analyses. For better whole-brain coverage, we also made a 90% group-specific mask. Before calculating functional connectivity, we first generated an individual-specific functional brain mask that included only voxels (in MNI standard space) present in each participant. We then generated a group-specific mask that included all voxels present in at least 90 percent (90%) of participants to ensure common coverage. This was then further constrained by a 99% gray-matter probability mask.

2.4.3. Homotopic FC

Homotopic FC was computed in two manners: (1) voxel-wise mirrored homotopic connectivity (i.e., VMHC) as developed and provided by Zuo et al. (2010), by registering the resting-state functional volumes onto a symmetric anatomical template and then calculating the Pearson's correlation coefficients (functional connectivity) of BOLD signals between the mirror-symmetric interhemispheric voxels, i.e., the individual VMHC map; (2) a less fine-grained ROI-wise functional homotopy, by registering the resting-state functional volumes to a recently validated homotopic brain parcellation based atlas (AICHA) (Joliot et al., 2015), which parcellates the brain into 384 parcels (192 homotopic pairs) based on clustering algorithms. The correlation coefficients were then z-score transformed.

2.4.4. Seed-based FC

Seed-based FC was computed based on the 16 significant clusters of between-group VMHC comparison (Table 2 & Fig 2). The seeds were 6-mm radius spheres centered at peak coordinates from the significant clusters: bilateral putamen (MNI coordinates: $X = \pm 24$, $Y = 9$, $Z = -9$), bilateral supramarginal gyri (MNI coordinates: $X = \pm 63$, $Y = -33$, $Z = 27$), bilateral planum temporale (MNI coordinates: $X = \pm 57$, $Y = -12$, $Z = 6$), bilateral opercular (MNI coordinates: $X = \pm 39$, $Y = 6$, $Z = 9$), bilateral lateral occipital (MNI coordinates: $X = \pm 42$, $Y = -60$, $Z = 51$), bilateral postcentral gyri/PMC (MNI coordinates: $X = \pm 48$, $Y = -12$, $Z = 36$), bilateral postcentral gyri (MNI coordinates: $X = \pm 6$, $Y = -36$, $Z = 57$), and bilateral superior parietal lobules (MNI coordinates: $X = \pm 42$, $Y = -42$, $Z = 51$). These additional seed-based functional connectivity analyses were performed using the DPABI toolbox with conventional correlation analysis.

Table 2
Brain areas with significantly different VMHC between patients vs. controls ($p < 0.05$, FDR voxel-wise corrected).

Regions	MNI coordinates			Voxels	BA	*T* values
	x	y	z			
Putamen	± 24	9	−9	27	–	−6.892
Supramarginal gyri	± 63	−33	27	40	40	−8.203
Planum temporale	± 57	−12	6	22	43/22	−8.092
Opercular cortices	± 39	6	9	34	13	−7.345
Posterior parietal cortices	± 42	−60	51	16	40/7	−6.505
Postcentral gyri/PMC	± 48	−12	36	35	6/4/3	−6.993
Postcentral gyri	± 6	−36	57	12	5	−6.868
Superior parietal lobules	± 42	−42	51	10	40	−6.489

Table 2 shows all local maxima. x, y, and z = MNI coordinates. Abbreviations: BA: Brodmann's area; T-value: the voxel of maximal intensity in this cluster; MNI: Montreal Neurological Institute; x, y, z: coordinates of primary peak locations in the MNI space. The threshold was set at voxel $p < 0.05$, FDR corrected. These results were reported with BSPMVIEW (http://www.bobspunt.com/software/bspmview/).

2.4.5. Homotopic SC

Homotopic SC was defined as white matter microstructural connectivity between each homotopic pair, including mean fractional anisotropy (FA), fiber number, and fiber length, using the deterministic tractography algorithm (Descoteaux et al., 2009). Processing was performed by using the FMRIB Software Library (FSL, https://www.fmrib.ox.ac.uk/fsl), the Pipeline for Analyzing braiN Diffusion imAges (PANDA, https://www.nitrc.org/projects/panda) (Cui et al., 2013), and MATLAB 2013a under a Linux-Ubuntu environment. The main steps included: (1) motion and eddy current artifacts correction; (2) brain extraction; (3) diffusion tensors calculation, in which the resulting FA volume of each subject was then registered to the FMRIB58_FA template using the FSL nonlinear registration tool FNIRT to obtain the warp field from native to standard space; (4) the nonlinear warp was initialized with an affine registration generated with the FSL linear registration tool FLIRT; (5) deterministic whole-brain streamline counts were generated using the fiber assignment by continuous tracking algorithm using the Diffusion Toolkit (trackvis.org/dtk) and TrackVis (www.trackvis.org); parameters included a 35° angle threshold, 20 seeds were placed in every voxel and a minimum streamline length of 20 mm was used. Network nodes were based on the 192 homotopic pairs (a total of 384 cortical and subcortical regions) comprising the AICHA atlas. The AICHA was mapped to an individual's native space using the inverse of the warp field previously computed. Each individual's network was represented with a symmetric 384 × 384 connectivity matrix. Each element of the connectivity matrix was populated with the number of streamlines between the corresponding pair of regions (streamline count), which served as a measure of inter-regional connection strength. The resultant average fiber FA, fiber number, and fiber length between each homotopic pair were imported into the SPSS 16.0 (SPSS Inc., Chicago, IL, USA) for further statistical analysis.

2.4.6. Brain perfusion and quantification of brain lesions

Brain perfusion was assessed with the PASL data using SPM12-based batch scripts ASLtbx (https://cfn.upenn.edu/~zewang/ASLtbx.php) including motion correction, temporal filtering, coregistration and spatial normalization, CBF image generation, and 6-mm spatial smoothing for subsequent group statistics.

We also calculated cerebral microhemorrhages and WMH by using

the SWI, FLAIR, and T1-weighted images. After visual inspection, brain lesions were automatically identified to create lesion maps for each individual's SWI and FLAIR images. The LST (www.applied-statistics.de/lst) for SPM12 were used to spatially normalize each individual's SWI and FLAIR lesion maps to the MNI152 template.

2.4.7. Brain behavior relationship

To examine whether there were any associations between the changes of VMHC and behavioral assessments in patients with SACS, we conducted Pearson's linear correlation analyses between behavioral assessments and mean VMHC values within each significant cluster. To explore the contribution of parenchymal lesion load to the VMHC, we also performed a correlation analysis between the VMHC and the WMH in the patients with SACS. All correlations were Bonferroni corrected at a significance level of $p < 0.05$.

2.4.8. Results verification and replication

We repeated the VMHC analysis using a range of Gaussian kernel (FWHM) values (4, 6, 8, 10, and 12 mm) and found that our results were robust. To examine the extent to which the patients could be discriminated from the controls based on the inter-group differences of VMHC, we applied a linear support vector machine (SVM) classification to the VMHC maps using the Pattern Recognition for Neuroimaging Toolbox (PRoNTo; www.mlnl.cs.ucl.ac.uk/pronto). To assess model performance, we applied a leave one-out cross-validation scheme. Under this cross-validation strategy, the classifier's accuracy was computed by leaving one subject out at a time and predicting this subject's group label based on a training set that includes all remaining subjects. Permutation testing was used to estimate the null distribution and examine the statistical significance of the classification accuracy (N permutations = 10,000; $p < 0.05$).

2.5. Statistical analysis

For all clinical variables, inter-group statistics were carried out using SPSS 16.0 (SPSS Inc., Chicago, IL) with a significance level set at $p < 0.05$. For the imaging measures, independent two-sample t-tests were used for functional connectivity and CBF, and nonparametric analyses were used for voxel-wise WMH and SWI analyses. These imaging measures were corrected using either voxel-wise false discovery rates (FDR) correction ($p < 0.05$) or cluster-level family-wise error (FWE) correction (voxel $p < 0.001$ and cluster $p < 0.05$) and controlled for age, gender, and head motion parameters (mean frame displacement).

2.6. Distribution of functions through the resulting t statistic VMHC

Finally, to examine brain functions subserving the significant clusters that showed between-group differences in the VMHC, we searched for research terms in the *NeuroSynth* database (www.neurosynth.org) (Yarkoni et al., 2011). A total of 32 terms were selected, and the corresponding brain activation regions were binarized into masks. The terms included “somatosensory, pain, motor, movements, noxious, motor imaginary, execution, action, auditory, speech production, speech, dorsal premotor, hands, listening, emotional, visual, working memory, stroke, language, default mode, semantic, reading, memory, autobiographic memory, dementia, encoding, episode memory, eye, face, navigation, tapping, and visual word”, etc. The statistical T map of VMHC was then binned into 5 percentile increments with its T values organized from most negative to most positive. These 20 gradient divisions form the heat map matrix of the topographies and the Z values of the topic terms. These terms were then ranked based on their statistical association with gradient T values for visualization. Heatmap colors encode the strength of correlation between each equally divided part of the VMHC T map and the Z statistic associated with the topic terms. The overall data processing flow is shown in Fig. 1

3. Results

3.1. Participants

We excluded five patients due to excessive head motion. Therefore, 19 patients and 24 controls were included in the final sample. Cognitively, SACS patients were severely impaired on recall tasks (both $p < 0.005$), and had considerably lower global cognition (subscales from MMSE and MoCA; $p < 0.05$), memory (memory subtest from verbal memory test, forward and backward digit span; $p < 0.05$), and executive function (subtest from Digit symbol; $p < 0.05$). Pathologically, patients with SACS had significantly higher WMH loads (ratio between WMH size and total brain size, WMH volumes, and WMH number, $p < 0.005$). See Table 1 for more detailed information.

3.2. Voxel-wise functional homotopy

Significant reductions of VMHC in bilateral putamen, lateral parietal lobules, premotor, primary somatosensory, planum temporale, and opercular cortices (voxel-wise $p < 0.05$, FDR corrected; Table 2 & Fig. 2A) were found in patients with SACS. These results were generally consistent with the comparison between patients with SACS and the independent sample of elderly HCs ($n = 84$) from the validation dataset (voxel-wise $p < 0.05$, FDR corrected; Fig. 2B).

3.3. ROI-based functional homotopy

As a complement to the voxel-wise analyses, we additionally calculated the ROI-wise homotopic FC based on the AICHA atlas (Fig. 3A), which yielded 192 homotopic links (Fig. 3B). Similar results for ROI-wise homotopy were found to that of the voxel-wise analysis (Fig. 3C). These included reductions of homotopic connectivity within the salience, frontoparietal, dorsal attention, and somatomotor networks (Fig. 3C; $p < 0.05$, FDR corrected).

3.4. Seed-based FC

Using the time courses extracted from the 16 significant clusters in the primary analysis of VMHC (as shown in Fig. 2A), we examined the functional integration of these clusters with the rest of the brain. Significant clusters (Fig. 4) of seed-based FC were identified and classified as part of the default, somatomotor, salience, executive, or dorsal attention network (Fig. 5).

3.5. Homotopic SC

Based on the deterministic tractography, we obtained three indices of structural connectivity for tracts connecting these homotopic brain regions (AICHA atlas): mean FA, fiber number, and fiber length. Decreased mean FA values between bilateral superior frontal, superior parietal, paracentral, and hippocampal regions (all survived Bonferroni corrections, with $p < 0.05$) were found. Reduced fiber length between bilateral superior parietal, superior frontal, and paracentral regions (survived Bonferroni correction, with $p < 0.05$) were found. Reduced fiber number between bilateral superior parietal, paracentral, and hippocampal regions ($p < 0.05$, uncorrected) were found (Table 3).

3.6. Results validation and SVM-based machine learning

To ensure that our findings were robust and not dependent upon the selection of Gaussian kernels, we repeated the VMHC analysis using a range of FWHM values (4, 6, 8, 10, and 12 mm), and found that the results were generally consistent (Fig. 6). Nevertheless, larger smoothing kernels resulted in more extensive significant clusters as well as additional results in the default mode network (DMN), i.e., the posterior cingulate cortex and ventral medial prefrontal cortex, when

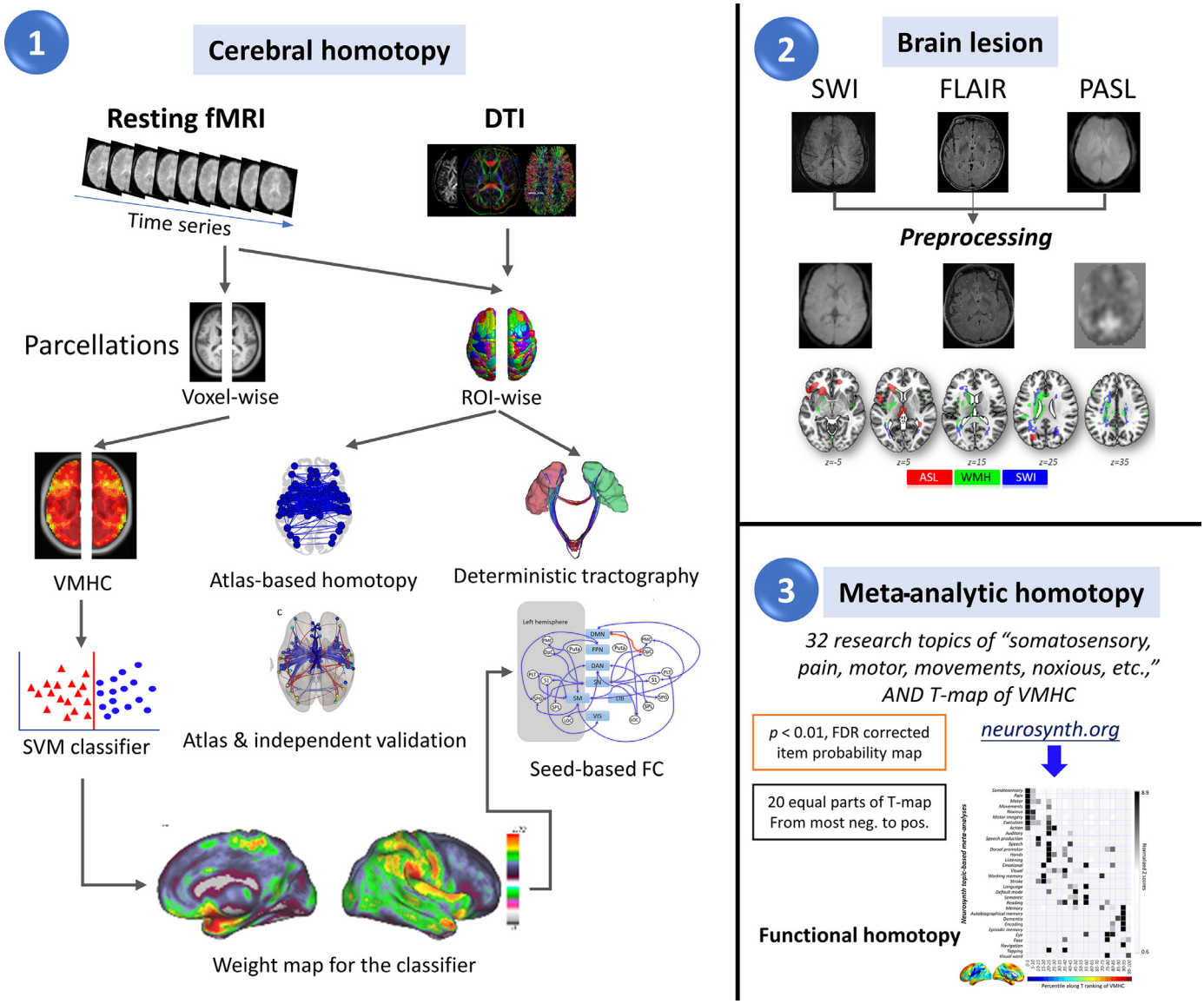

Fig. 1. Schematic overview of (1) homotopic connectivity, (2) brain lesion qualification, and (3) Meta-analytical heatmap.

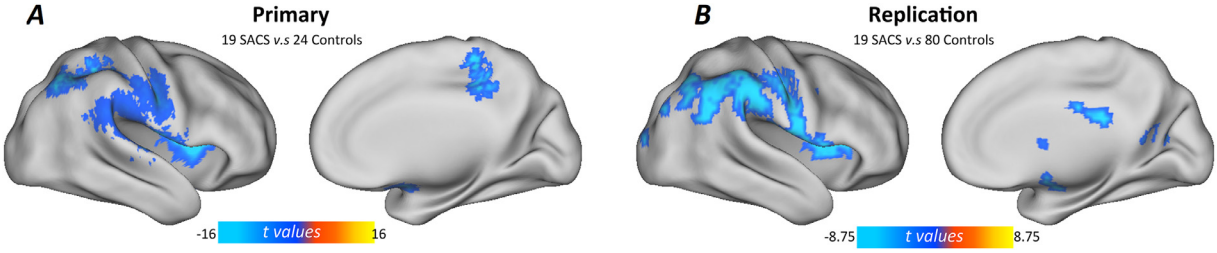

Fig. 2. Between-group differences in voxel-wise homotopic connectivity. **(A).** Primary results of between-group differences in voxel-wise homotopic connectivity, from a cohort of 19 patients with SACS versus 24 comorbidities- and demographically- matched controls ($p < 0.05$, voxel-wise FDR corrected). **(B).** A validation of between-group comparison, from the cohort of 19 patients versus an independent dataset of 84 matched elderly controls ($p < 0.05$, voxel-wise FDR corrected).

the smoothing kernel was greater than or equal to 10 mm.

Due to our relatively small sample size, it was important to assess the reliability of the results. To this end, we used cross-validation and SVM-based machine learning for classification. Balanced accuracy: 95.29% (p_{BA} = 0.02); total accuracy 95.53%, class accuracy (CA) 94.74%, 95.83% (p_{CA} = 0.02), class predictive values were 94.74% and 95.83% (Fig. 7).

3.7. Qualification of brain lesions and perfusion

For the PASL-derived CBF, patients with SACS showed significant hypoperfusion in the left pars opercularis, left orbitofrontal, bilateral thalami, right dorsal anterior cingulate, and left middle occipital cortices (Table 4). For the voxel-wise comparison of SWI, we identified several brain clusters with hypointensity in patients, including frontal, parietal, temporal, and periventricular white matter (Table 5 & Fig. 8).

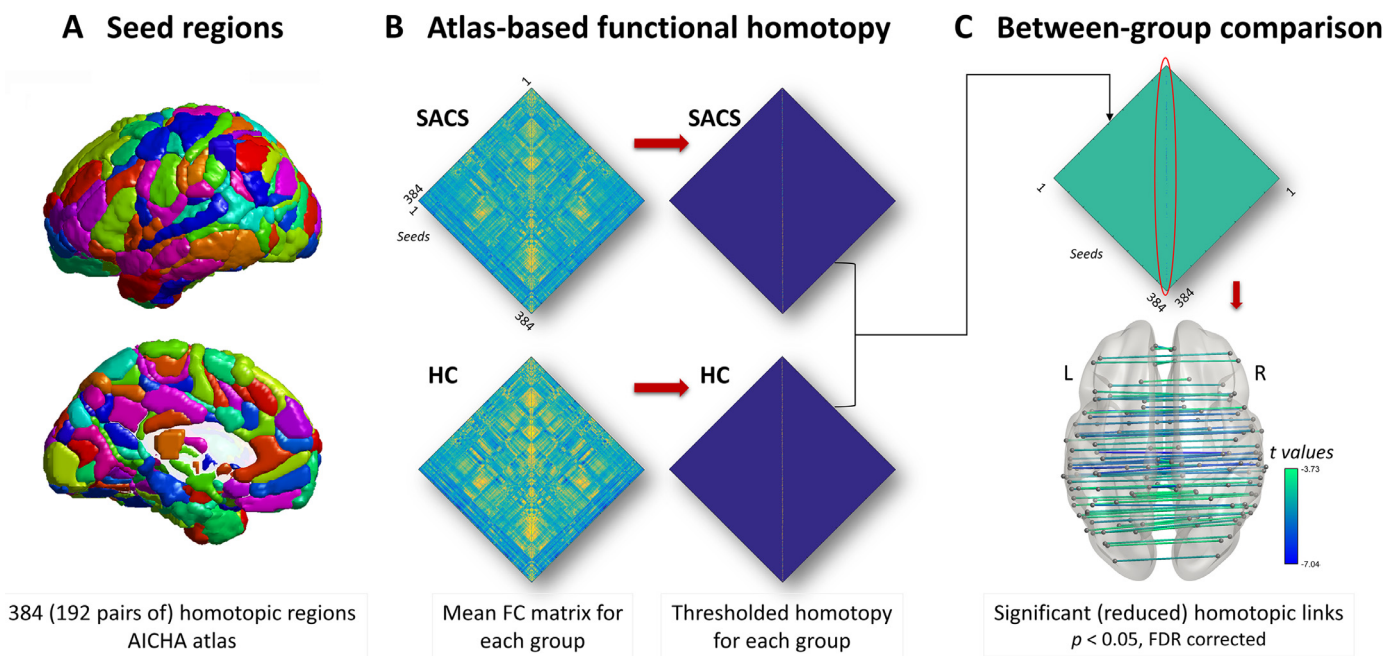

Fig. 3. ROI-based homotopic connectivity. (A). Seed ROI selection from the AICHA atlas. Each hemisphere includes 192 homotopic regions. **(B).** Functional connectome and homotopic connectivity. First, functional connectivity matrix seeding from the AICHA atlas were thresholded into individual homotopic matrices. Individual homotopic matrices were then input into the second statistic model. **(C).** Between-group comparison of the homotopic connectivity. Matrix and surface-view of homotopic connectivity between each homotopic ROI. These results were corrected at a connection level, $p < 0.05$ with FDR correction.

For WMH measured by T2-FLAIR, we found that the distribution and number of WMH in SACS patients were significantly higher than the controls, especially in the periventricular areas. Areas of overlap included the left inferior frontal gyrus (Brodmann area 22), the left inferior parietal lobule (Brodmann areas BA40/2), the left precentral gyrus/postcentral gyrus, the left putamen, the left medial frontal gyrus (Brodmann area 6) and the left middle temporal gyrus. To aid in visualization, the three suprathreshold statistical parameter maps are

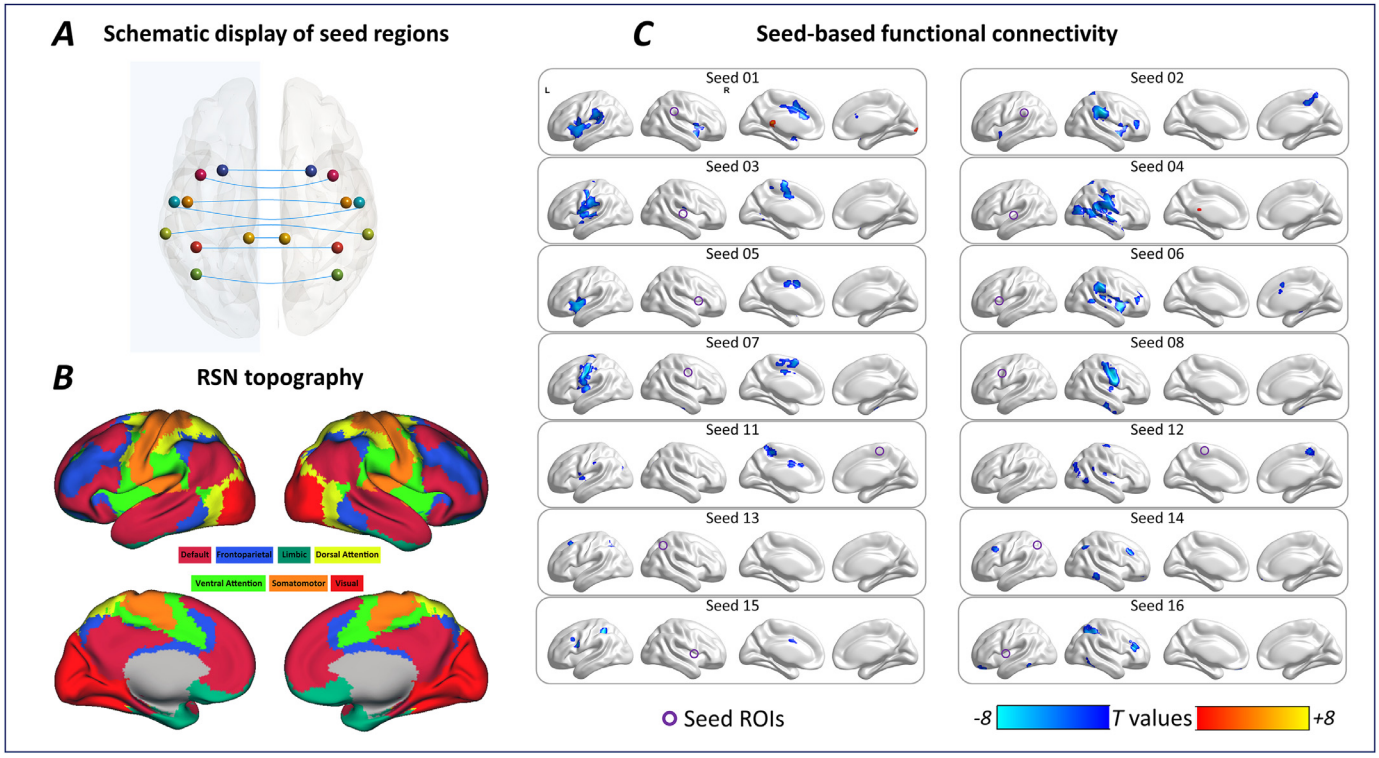

Fig. 4. Seed-based functional connectivity. (A). Schematic display of the selection of seed regions. Each sphere represents a seed region, and the lines connecting them represent homotopic functional connectivity with significant inter-group differences. **(B).** The topography of the seven average large-scale resting brain networks provided by Yeo et al. (2011). **(C).** Between-group comparison of seed-based functional connectivity with seeds selection from A. Purple circle represents a seed region. These results were FDR corrected at a voxel-level, $p < 0.05$. Here, we only list the seed-based FC with significant inter-group differences and do not include the seeds with only homotopic FC differences. Theoretically, each seed should yield at least one significant cluster with its homotopic region.

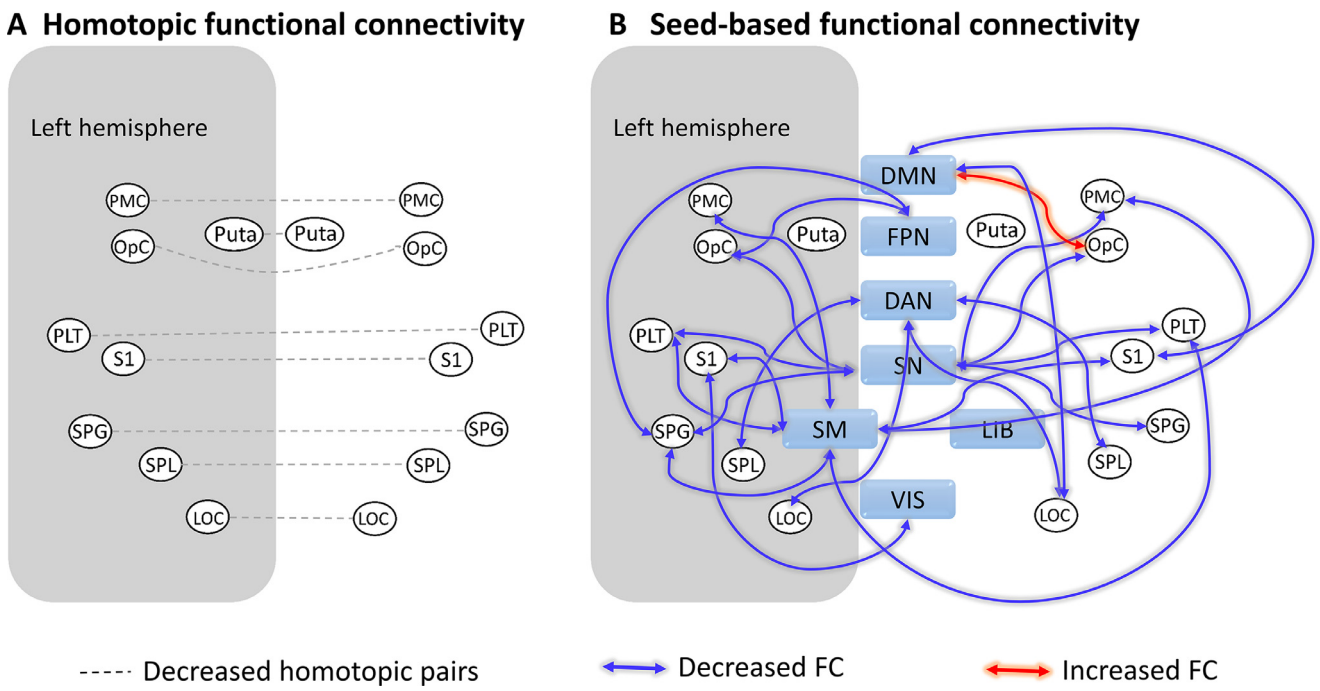

Fig. 5. Schematic of significant (decreased) homotopic pairs and seed-based functional connectivity. (A). Schematic of decreased homotopic functional connectivity (dashed gray lines) and ROI seeds (gray circles). **(B).** Between-group comparison of seed-based functional connectivity with seed selection from (A). Their inter-group results (double arrow lines) were assigned to 7 average large-scale intrinsic brain networks provided by Yeo et al. (2011). These results were FDR corrected at a voxel-level, $p < 0.05$. Abbreviations: PMC, premotor cortex ($X = \pm 48$, $Y = -12$, $Z = 36$); OpC, operculum/insular ($X = \pm 39$, $Y = 6$, $Z = 9$); Puta, putamen ($X = \pm 24$, $Y = 9$, $Z = -9$); PLT, planum temporale ($X = \pm 57$, $Y = -12$, $Z = 6$); S1, primary somatosensory cortex ($X = \pm 6$, $Y = -36$, $Z = 57$); SPG, supramarginal gyrus ($X = \pm 63$, $Y = -33$, $Z = 27$); SPL, superior parietal lobule ($X = \pm 42$, $Y = -42$, $Z = 51$); LOC, lateral occipital cortex ($X = \pm 42$, $Y = -60$, $Z = 51$); DMN, default mode network; FPN, fronto-parietal network; DAN, dorsal attention network; SN, salience network; SM, somatomotor network; LIB, limbic network; VIS, visual network.

Table 3
Between-group comparison in homotopic structural connectivity.

Homotopic Regions	*T values*		
	Fiber Length	*Mean FA*	*Fiber number*
G_Frontal_Sup_Medial-3	−5.93*	−5.86*	N.S.
G_Frontal_Sup-2	N.S.	−4.88*	N.S.
G_Hippocampus-2	−2.78	−4.01*	−2.96
G_Paracentral_Lobule-2	−4.41*	−4.4*	−3.12
G_Parietal_Sup-5	−4.56*	−4.73*	−2.04

Homotopic SC was measured by deterministic tractography of DTI with the AICHA atlas. The significance level was routinely set to $p < 0.05$, but we only listed the results that passed through Bonferroni correction, corresponding to $p < 0.05/184 \approx 0.0003$, marked with an asterisk. N.S., non significant.

shown superimposed onto the standard MNI152 brain template (Fig. 8).

3.8. Association of VMHC to behavioral and lesion parameters

We first quantified the relationship between the VMHC and behavioral measurements. VMHC between the bilateral supramarginal gyri (SACS patients, $n = 19$, $r = 0.591$, $p = 0.0078$; all subjects, $r = 0.538$, $p = 0.0002$;) and the bilateral superior temporal gyri (SACS patients, $n = 19$, $r = 0.664$, $p = 0.0019$; all subjects, $r = 0.651$, $p < 0.001$) were both positively correlated with delayed recall (Fig. 9). We next assessed the relationships between WMH loads and the cognitive variables, as well as WMH loads and VMHC. We did not find any significant correlation between the WMH loads (including WMH number, absolute WMH size, and relative WMH volume with TIV) and the behavioral variables. However, the corrected WMH loads (i.e., the ratio of WMH size and total intracranial volume) was significantly negatively corrected with the VMHC between the bilateral angular (SACS patients, $n = 19$, $r = -0.675$, $p = 0.002$; all subjects, $r = -0.644$, $p < 0.001$), insula (SACS patients, $n = 19$, $r = -0.715$, $p = 0.001$; all subjects, $r = -0.610$, $p < 0.001$), supramarginal gyri (SACS patients, $n = 19$, $r = -0.776$, $p < 0.001$; all subjects, $r = -0.678$, $p < 0.001$), and bilateral putamen (SACS patients, $n = 19$, $r = -0.742$, $p < 0.001$; all subjects, $r = -0.632$, $p < 0.001$) (Fig. 9).

3.9. Distribution of functions through the resulting T statistic VMHC

Finally, we examined whether the functional processes ascribed to the resulting T statistic VMHC specifically involved sensory inputs, perception, and concrete cognitive functions. We performed meta-analytic decoding using the *Neurosynth* database to correlate the research terms and the T statistical maps. Top terms exhibiting the strongest associations included basic functions, such as “somatosensory, pain, motor, movements, noxious, motor imaginary, execution, action, auditory, speech production.” (Fig. 10).

4. Discussion

4.1. Summary of findings

Our investigation demonstrates robust homotopic FC reductions in patients with SACS in brain regions dominated by the middle cerebral arteries, especially in the Perisylvian fissure. These involved regions span across the large-scale intrinsic networks including somatomotor, salience, dorsal attention, and orbitofrontal-limbic. Results showed that the significantly reduced homotopic FC can be partially explained by white matter hyperintensity size. Further association analyses suggested that decreased homotopic FC in these brain regions is most closely associated with delayed memory recall, sensorimotor processing, and other simple cognitive functions. These results suggest that SACS may preferentially affect lower-order cognitive processes, while

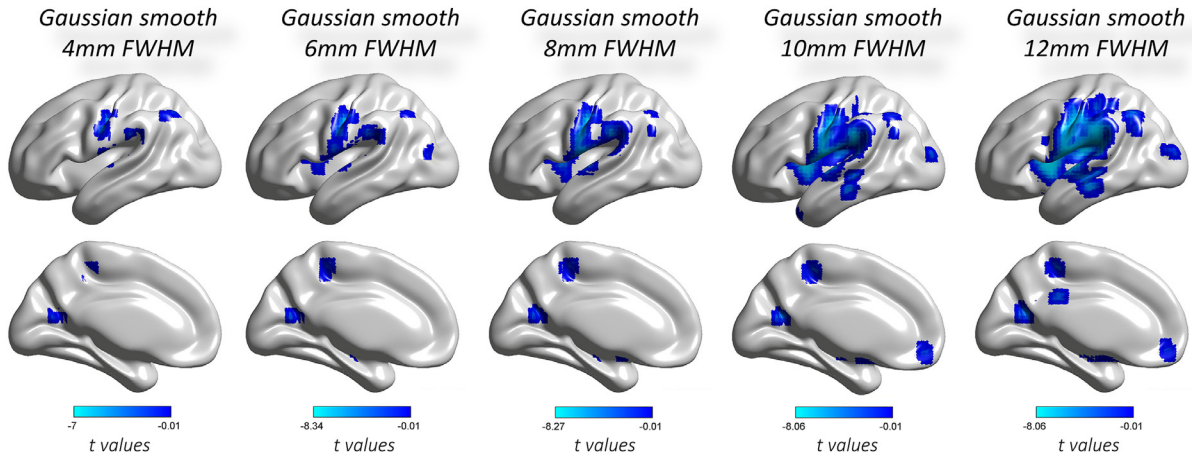

Fig. 6. The effects of different FWHM Gaussian smoothing kernels on between-group comparison of VMHC. Overall, the selection of different FWHM Gaussian smoothing kernels yielded similar results. At the same time, oversmoothing generated additional results in the medial prefrontal (10 and 12 mm FWMH) and posterior cingulate regions (12 mm FWMH). These results were FDR corrected at a voxel-level, $p < 0.05$.

the higher-order systems, including regions in the DMN that subserve abstract thought, appear to be least impacted. However, decreased homotopic FC within the DMN may be a precursor to vascular dementia. Thus, measurements of homotopic FC may provide clinical utility by noninvasively tracking the progression of downstream brain damage following SACS.

Prominent homotopic FC is a significant phenomenology in human (Stark et al., 2008; Zuo et al., 2010), non-human primates (O'Reilly et al., 2013), and some other known mammals' brains (Layden et al., 2019). Reports on agenesis (Tyszka et al., 2011), absence (Split-brain) (Johnston et al., 2008), and resection (callosotomy) (Pizoli et al., 2011; Roland et al., 2017) of the corpus callosum suggest that this prominent homotopy in the association (higher-order) cortices is heavily dependent on the integrity of the corpus callosum, while homotopy in the primary cortices may be supported via multiple extracallosal pathways.

Homotopic FC exhibits increasing primary cortical integration (i.e., increasing homotopic connectivity) and higher-order segregation (i.e., decreasing homotopic connectivity) across lifespan development (Zuo et al., 2010), and has been implicated in several neuropsychiatric and neurological conditions (Carter et al., 2010; Hoptman et al., 2012; Kelly et al., 2011; Li et al., 2017). Our current findings show significant homotopic reductions in patients with SACS, specifically, in the topographies of the Perisylvian fissure, temporal-occipital-parietal conjunction, lateral parietal, insular, and basal ganglia. These regions comprise parts of the somatomotor, dorsal attention, frontoparietal, and

Table 4
Between-group comparison on PASL-based CBF (SACS v.s. Controls).

Regions	MNI coordinates			Voxels	BA	*T* values
	x	y	z			
Left middle occipital gyrus	−26	−74	24	196	19	−3.75
Left pars opercularis	−52	12	−2	1066	48	−3.18
Left orbitofrontal cortex	−44	30	−8	1066	47	−2.98
Thalamus	34	−48	4	207	–	−3.00
Right dACC	14	44	−4	140	32	−2.99

shows all peak coordinates. Abbreviations: BA: Brodmann's area; *T*-value: the voxel of maximal intensity in this cluster; MNI: Montreal Neurological Institute; x, y, z: coordinates of primary peak locations in the MNI space; dACC, dorsal anterior cingulate cortex. The threshold was set at a corrected voxel $p < 0.001$, cluster level $p < 0.05$, FWE cluster-level corrected. These results were reported with BSPMVIEW (http://www.bobspunt.com/software/bspmview/).

salience networks, whose functions putatively subserve somatosensory, memory, attention, executive, fine motor, and visceral processes (also see the metanalytic decoding). These findings are generally consistent with earlier reports on both human and rodents (Cheng et al., 2012; Lin et al., 2014; Panczykowski et al., 2014) and our recent studies (Wang et al., 2017).

Our results of the VMHC were validated through three additional analyses (preprocessing scheme, independent controls, and SVM-based cross validation, Figs. 2, 3, 6, and 7), which demonstrated the robustness of our results, and together suggested that VMHC reduction is an

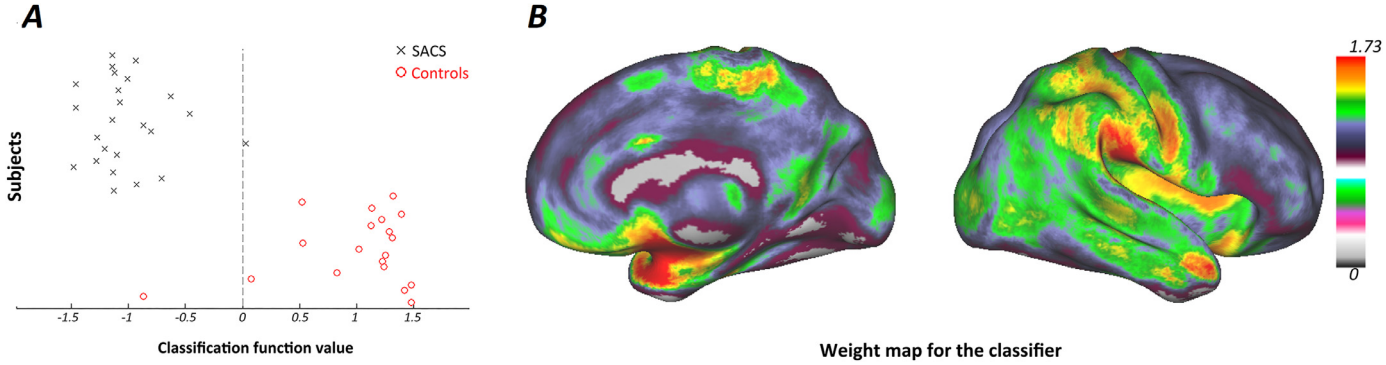

Fig. 7. Multivariate pattern classification. (A). Scatter plot depicting the support vector machine classification results within the suprathreshold mask. Balanced accuracy (BA): 95.29%; dashed line is the function value cut-off between classes (0), leave-one-out cross-validation, $N_{permutations} = 10{,}000$, $p \leq 0.05$. Function values are plotted per fold (i.e., in this case, per subject). **(B)**. Whole brain weight map for the classifier, depicting the relative contribution of the voxel to the decision function. Total accuracy 95.53%, BA *p* value 0.02, class accuracy (CA) 94.74%, 95.83%. CA *p* value 0.02, class predictive value 94.74%, 95.83%.

Table 5
Brain areas with significantly different SWI intensities between patients vs. controls ($p < 0.05$, FWE cluster-level corrected).

Regions	MNI coordinates			Voxels	BA	*T* values
	x	y	z			
Left Caudate	−15	−4	24	21,952	–	−5.10
Left Hippocampus	−31	−13	−10	21,952	20	−4.426
Left SMA	−4	−9	58	330	6	−4.37
Left Thalamus	−4	−24	11	21,952	–	−4.23
Right Superior Temporal	44	−8	−8	604	48	−4.11
Left Inferior Parietal	−51	−39	58	1042	2/40	−3.961
Right Supramarginal gyrus	64	−24	31	284	2	−3.72
Right Parietal Operculum	47	−25	21	268	48	−3.67
Left Supramarginal gyrus	−45	−33	25	1141	48	−3.63
Right Supramarginal gyrus	16	−25	35	560	48	−3.65
Right Fusiform	38	−48	−21	307	37	−3.20

Between-group comparison on SWI (SACS v.s. Controls). Table 5 shows all peak coordinates. Abbreviations: BA: Brodmann's area; *T*-value: the voxel of maximal intensity in this cluster; MNI: Montreal Neurological Institute; x, y, z: coordinates of primary peak locations in the MNI space; dACC, dorsal anterior cingulate cortex. The threshold was set at a corrected voxel $p < 0.001$, cluster-level $p < 0.05$, FWE cluster-level corrected. These results were reported with BSPMVIEW (http://www.bobspunt.com/software/bspmview/).

important feature of SACS patients. As noted in the primary analysis (Fig. 2), the main results are largely consistent across smoothing kernels (Fig. 6). However, as the smoothing kernel increased, or possibly due to a threshold effect, new brain regions with significant between-group difference emerged, particularly those located in the medial portions of the DMN (i.e., the posterior cingulate and ventromedial prefrontal cortices) (Raichle, 2015). These results suggest the possibility that an early change in SACS initiates a marginal change in DMN, which might subsequently involve the core regions within the DMN, speculation that coincides with vascular dementia and patterns of disease propagation (Dichgans and Leys, 2017). In addition, we found that in the classification of VMHC differential brain regions, one elderly control fell into the "patient" class, which may indicate undetected hypoperfusion in subpopulations of healthy older adults.

Our results on homotopic connectivity can be considered in the context of ischemia-hypoxia and hemodynamic changes. Reduced CBF and impaired cerebrovascular reactivity have been consistently reported in asymptomatic higher-grade ICA stenosis patients (Chen et al., 2017; Hartkamp et al., 2017; Hu et al., 2018), particularly in the anterior circulation of the affected hemisphere (Silvestrini et al., 2000). Evidence suggests that similar homotopic reductions, as shown in the current study, can be seen in acute cerebral hypoxia (experimental hypercapnia) (Marshall et al., 2015). Surprisingly, our examination of PASL-based CBF did not show prominent reductions in the brain territories dominated by the MCA in the patients with SACS. We speculate that this might be due to blood transit delays in severe ICA stenosis with a single labeling/inversion time. This consideration is both supported by previous reports (Bokkers et al., 2009; Hendrikse et al., 2004), and confirmed by our unpublished analysis of lag structure on resting-state time series, with average time delays of ~ 2 s. This asymmetrical change results in neural propagation and phase delay (mismatch), which corresponds to the dramatically decreased functional homotopy measured by resting-state BOLD time series.

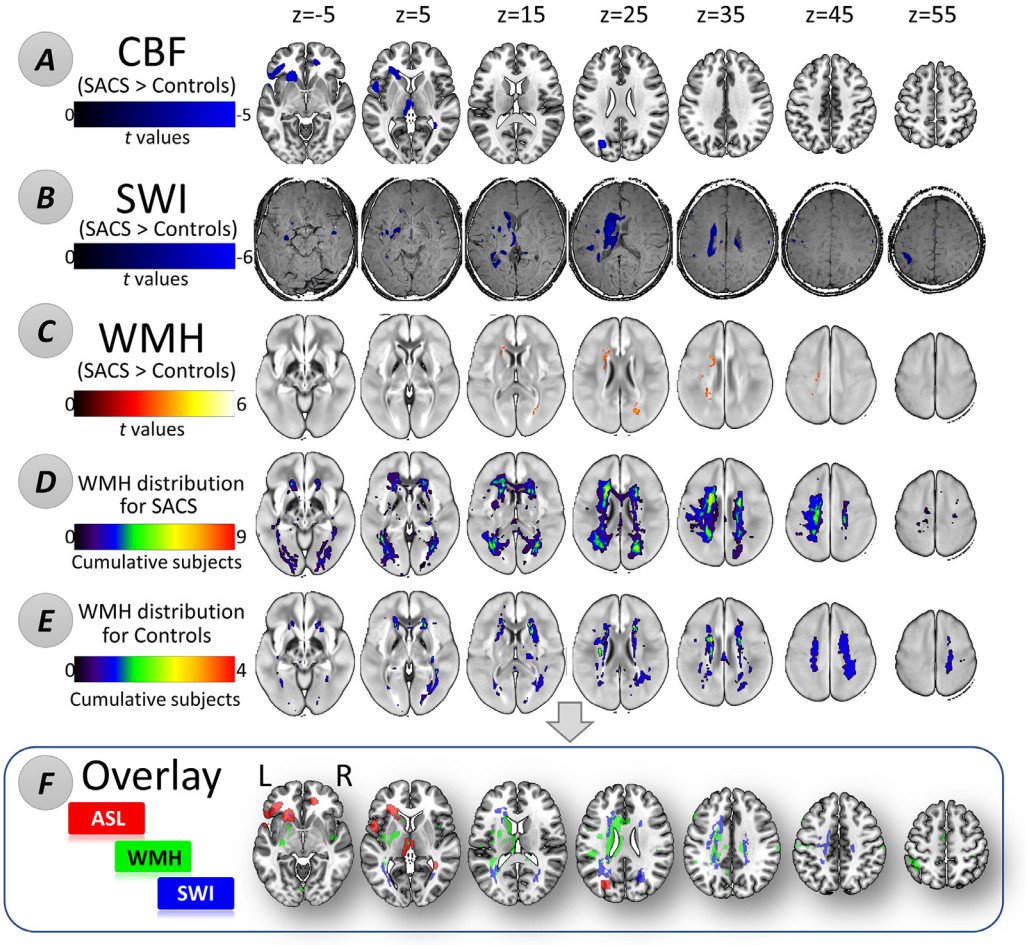

Fig. 8. Qualification of brain lesions and hypoperfusion. (A). Between-group comparison on CBF. The blue tone indicates significant brain regions with hypoperfusion in the patients with SACS. No significant hyperperfusion was found. **(B).** Between-group comparison in SWI signal intensities. The blue tone indicates significant low-signal foci in the patients with SACS. **(C).** Between-group comparison on T2-FLAIR based WMH. The hot tone indicates significant brain regions with increased WMH in the patients with SACS. These results (A-C) were corrected by FWE cluster-level $p < 0.05$ and voxel-level $p < 0.001$. **(D).** Cumulative WMH distribution for the patients with SACS. From left to right (cold to hot hues), the color indicates number of subjects (up to 9) with WMH in the same brain region. **(E).** Cumulative WMH distribution for the healthy controls (HC). From left to right (cold to hot hues), the color indicates number of HC subjects (up to 4) with WMH in the same brain region. **(F).** Superimposed map of brain lesions and hypoperfusion. Suprathreshold between-group differences of PASL-based hypoperfusion (Red label), significant high load of WMH measured by FLAIR (Green label), and hypointensities measured by SWI (Blue label) in the patients with SACS. Their main overlapping areas include the left inferior frontal gyrus (BA 22), the left inferior parietal lobule (BA40/2), the left precentral gyrus/postcentral gyrus, the left putamen, the left medial frontal gyrus (BA6) and the left middle temporal gyrus. Abbreviations: L, left; R, right; BA, Brodmann area.

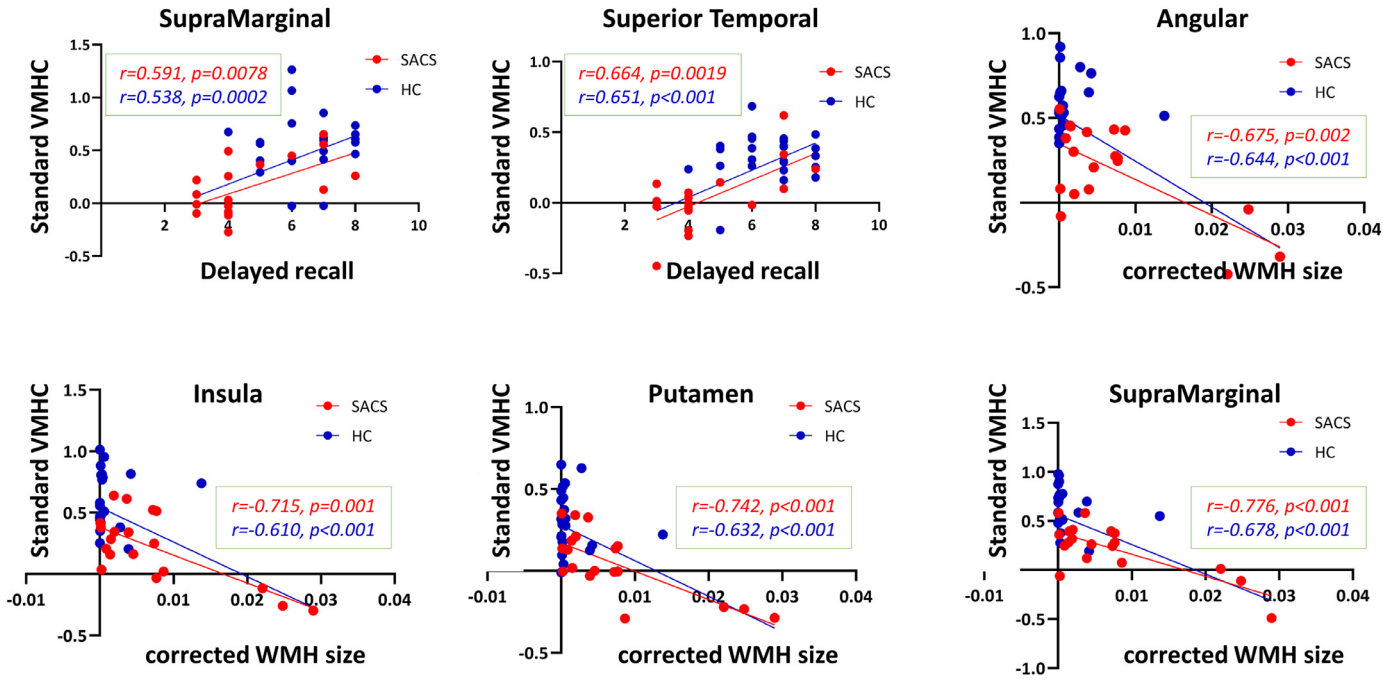

Fig. 9. Association with behavior. VMHC between the bilateral superior parietal lobules (SACS patients, $n = 19$, $r = =0.591$, $p = =0.0078$; all subjects, $r = =0.538$, $p = =0.0002$) and the bilateral superior temporal gyri (SACS patients, $n = 19$, $r = 0.664$, $p = 0.0019$; all subjects, $r = =0.651$, $p < 0.001$) were both positively correlated with delayed recall. The VMHC between the bilateral angular gyri (SACS patients, $n = 19$, $r = -0.675$, $p = =0.002$; all subjects, $r = -0.644$, $p < 0.001$), insula (SACS patients, $n = 19$, $r = -0.715$, $p = =0.001$; all subjects, $r = -0.610$, $p < 0.001$), supramarginal gyri (SACS patients, $n = 19$, $r = -0.776$, $p < 0.001$; all subjects, $r = -0.678$, $p < 0.001$), and bilateral putamen (SACS patients, $n = 19$, $r = -0.742$, $p < 0.001$; all subjects, $r = -0.632$, $p < 0.001$) were significantly negative correlated with the corrected WMH loads (i.e., the ratio of WMH size and total intracranial volume).

Organizationally, we note that SACS patients show prominent reductions in VMHC in the Perisylvian fissure, typically considered at the low-level of the functional hierarchy and anchored to sensory perceptions, motor actions, and physical fitness (Huntenburg et al., 2018; Margulies et al., 2016). Further, the angular, supramarginal, and superior temporal gyri—considered at a higher-level in the functional hierarchy—also showed significant reductions of VMHC, and were significantly correlated with memory, processing speed, and attention deteriorations. The mammalian cerebral cortex is a functional hierarchy with spatiotemporal organization. At the low-level of this hierarchy sit the primary sensorimotor cortices, with transmodal association cortices considered higher up and the DMN located near the apex (Huntenburg et al., 2018; Margulies et al., 2016). Movement from lower to higher in this functional hierarchy generally corresponds with concrete to abstract cognitive processing, respectively. From this perspective, patients with SACS primarily show decreased FC in low-level areas of this functional hierarchy, with corresponding limited impairment in the abstract cognitive functioning domain. Our observations and speculations are also consistent with previous reports (van Meer et al., 2010). For example, similar homotopic reductions can be seen in acute cerebral hypoxia (experimental hypercapnia) (Marshall et al., 2015), or stroke (van Meer et al., 2010), following the hierarchy from primary sensory-motor to higher-order cortices.

In addition to the spatial arrangement of VMHC reductions in patients with SACS, we identified significant relationships between VMHC and behavioral data, as well as VMHC with term-based meta-analytic brain functions. The supramarginal gyrus is variably assigned to the dorsal attention network or the DMN, and associated with memory, attention, and executive functions. The superior temporal gyrus is known to be involved in visuomotor integration (Iacoboni and Zaidel, 2004), while the insula and operculum are generally assigned to the salience network, an important role of which is interoceptive processing and large-scale intrinsic network coordination/switching (Michels et al., 2015). These brain regions and putative functions are consistent with the domains of cognitive impairment seen in SACS. To supplement and verify these results, we correlated the *T*-map of VMHC according to the absolute *T* value rank with the meta-analytical activation map of research items, and found that the severely affected brain areas (the top 10% *T* value) of the SACS patients were mainly related to basic somatomotor or concrete cognitive functions (Fig. 10), including the research topics of somatosensory, pain, motor, movements, noxious, motor imaginary, execution, action, etc. These results reinforce that SACS preferentially affects the lower hierarchy of the brain's functional organization, i.e., regions subserving somatomotor and simple cognitive functions, while areas further up on the hierarchy such as the DMN are least impacted.

Pathologically, SACS represents a type of silent cerebrovascular disease, which includes silent lacunar infarct, cerebral microbleeds, and WMH (van Veluw et al., 2017). To explain the underlying causes of the VMHC reductions, we further explored the relationship between the VMHC and white matter microstructural integrity, WMH load, and cerebral microbleeds. Using deterministic tractography, we found that only five of 192 homotopic regions showed significantly lower SC in the SACS patients, in the brain regions of superior medial frontal, hippocampus, paracentral, and superior parietal cortex. These regions are consistent with regions showing significant VMHC reductions. Moreover, among the three DTI indices, the difference in mean FA was the most significant, followed by fiber length, with fiber number being the least significant. These results suggest that mean FA may be a sensitive indicator that is more likely to reflect white matter damage in patients with SACS (Avelar et al., 2016; Baradaran et al., 2016). Despite the significant reduction in these significant homotopic structural connections, we believe that this does not account for the full scope of homotopic FC reductions observed, since the number of the homotopic pairs is disproportionally matched. We also identified hypointensities of SWI in the frontal, parietal, and temporal gray matter, and periventricular white matter regions in patients with SACS (Table 5 & Fig. 8). The distribution and number of WMH in SACS patients were

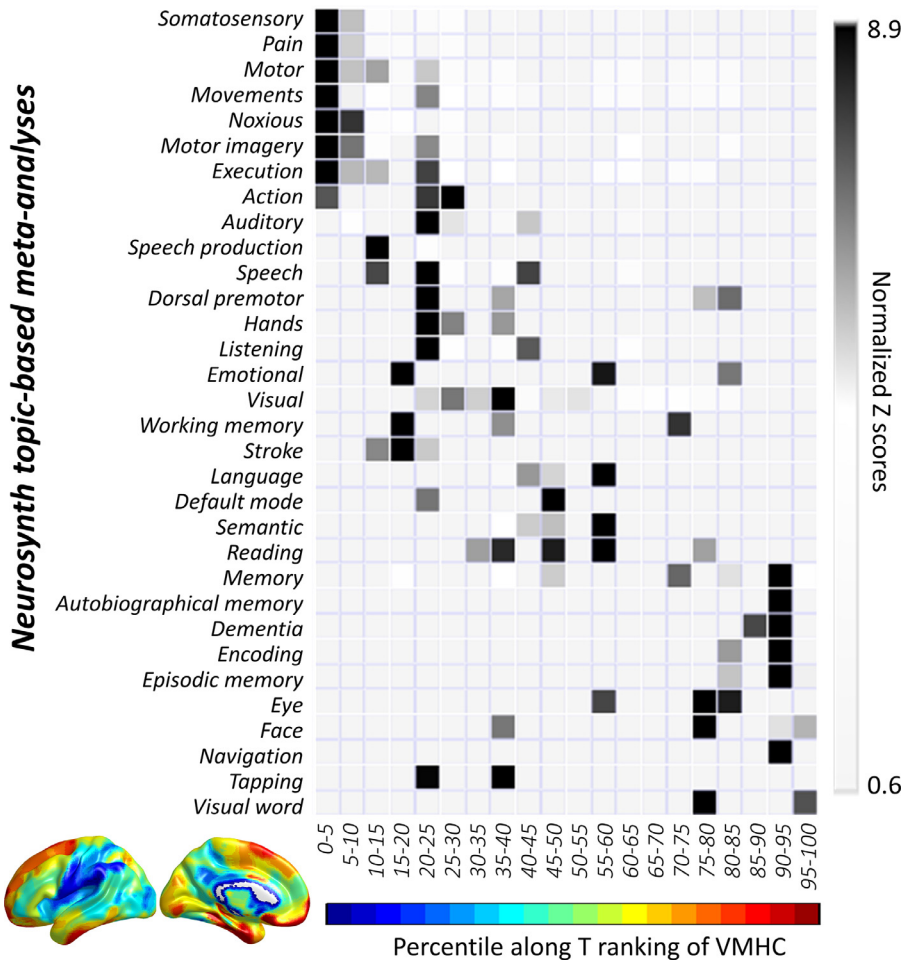

Fig. 10. Functional topographies and decreased homotopy. The meta-analytic decoding of brain functions through the *T* map of VMHC. Rows represent 20 equal parts through the VMHC *T* statistic map in its entire range. Columns represent the brain clusters of the 32 *NeuroSynth* terms that survived multiple comparison correction (voxel-wise $p < 0.01$, FDR corrected; $Z > 3.1$). The research terms are sorted by their *Z* values and anatomical foci through the *T* map. Heatmap colors encode the strength of correlation between each equally divided part of the VMHC *T* map and the research terms. The top association terms including "somatosensory, pain, motor, movements, noxious, motor imaginary, execution, action, speech production, and speech", are located in the top 15% of the between-group differences and also correspond to the significant clusters reported in the current study.

significantly higher than the matched healthy aging controls, especially in the periventricular areas. Furthermore, the VMHC between the bilateral angular, insula, and supramarginal gyri, and bilateral putamen were significantly negatively correlated with the corrected WMH loads (i.e., the ratio of WMH size and total intracranial volume) (Fig. 9). This suggests that the brain lesion load of SACS patients is higher than that of healthy controls, and may at least partially explain the reduction of functional connectivity. However, these relationships should be replicated and further investigated by future studies.

Regarding the application of VMHC in brain diseases, the reliability and validity of VMHC, and particularly the use of SACS as a potential biomarker, warrants additional investigations. A recent study has indicated that in the application of VMHC to gender differences, the intraclass correlation coefficient is roughly 0.44 (Chen et al., 2018), suggesting that the test-retest reliability and generalizability still needs to be explored in depth. However, in this study and previous studies, in the context of multiple white matter lesions, VMHC is a better indicator of heterogeneous brain disease. Recently, an important focus in the neuroimaging community is reliability and validity (Xing and Zuo, 2018; Zuo et al., 2019a; Zuo and Xing, 2014, 2019). In particular, in the last decade, the field has witnessed the escalation of multi-center, large-sample inter-individual data for exploring individual differences and obtaining general conclusions. Yet, still, the sample length of the intra-individual data is still relatively small, only a few minutes, showing poor reliability and validity. Therefore, future research should extend the scan times of intra-individual data and perform repeated-measurements of resting scans (Zuo et al., 2019b).

We must address the limitations of this study. Since this study was not primarily designed for the assessment of sensorimotor functions, we did not assess any brain-behavior relationships in the motor ability domain. Second, because a single-inflow-time pASL sequence was used, we may not be able to calculate individual CBF maps and mean transit time accurately. Third, the threshold effect of silent brain lesions and their relationship with functional connectivity are rather complicated, which is one of the active research topics in this field and one of the future research directions. Finally, due to the number of statistical items in this study, we used two of the most popular correction methods, voxel-wise FDR correction with $p < 0.05$, and voxel-wise uncorrected $p < 0.001$ with cluster-level FWE correction with $p < 0.05$. Although these are the most current recommended methods, the disadvantage is diminished localizing ability and sensitivity.

Conclusion

Homotopic FC alterations, specifically in the somatomotor, salience, dorsal attention, and executive systems are characteristic changes in patients with SACS. These results suggest that the SACS preferentially affects the lower tier of the functional hierarchy, while cognitive systems further up on the hierarchy (i.e., the default mode network) are least impacted by SACS, but may be a hallmark precursor to vascular dementia. Thus, measurements of homotopic FC may help to non-invasively track the progression of downstream brain damage following asymptomatic carotid stenosis.

Declaration of Competing Interest

All authors disclosed no relevant relationships.

Acknowledgement

We thank Prof. Yu-Feng Zang (Hangzhou Normal University) for his in-depth insights in methodology and discussion, as well as for years of consistent academic support. We thank Dr. Lindsay K. Knight (University of Louisville), Dr. Jingyi Fan (Wuhan University), Dr. Wei-Yin Liu (National Cheng Kung University), and Prof. James F. Burke (Boston, MA, US) for English editing. This study was supported by the National Natural Science Foundation of China (Grants No. 81771914, 81771819, and 81801068), National key research and development plan of China (Grants no. 2016YFC0100300 and 2017YFC0108803), Zhongnan Hospital of Wuhan University Science, Technology and Innovation Seed Fund(Projects cxpy2017048 and cxpy20160057), and the Fundamental Research Funds for the Central Universities (Projects 2042017kf0284 and 2016060605100525).

References

Anderson, J.S., Druzgal, T.J., Froehlich, A., Dubray, M.B., Lange, N., Alexander, A.L., Abildskov, T., Nielsen, J.A., Cariello, A.N., Cooperrider, J.R., 2011. Decreased interhemispheric functional connectivity in autism. Cerebral Cortex 21, 1134–1146.

Ashburner, J., 2007. A fast diffeomorphic image registration algorithm. Neuroimage 38, 95–113.

Avelar, W.M., D'Abreu, A., Coan, A.C., Lima, F.O., Fernando, C., 2016. Asymptomatic carotid stenosis is associated with gray and white matter damage. Int. J. Stroke 10, 1197–1203.

Baradaran, H., Mtui, E.E., Richardson, J.E., Delgado, D., Dunning, A., Marshall, R.S., Sanelli, P.C., Gupta, A., 2016. White matter diffusion abnormalities in carotid artery disease: a systematic review and meta-analysis. J. Neuroimaging Official J. Am. Soc. Neuroimaging 26, 481–488.

Biswal, B., Yetkin, F.Z., Haughton, V.M., Hyde, J.S., 1995. Functional connectivity in the motor cortex of resting human brain using echo-planar MRI. Magn. Reson. Med. 34, 537–541.

Bokkers, R.P., van der Worp, H.B., Mali, W.P., Hendrikse, J., 2009. Noninvasive MR imaging of cerebral perfusion in patients with a carotid artery stenosis. Neurology 73, 869–875.

Carter, A.R., Astafiev, S.V., Lang, C.E., Connor, L.T., Rengachary, J., Strube, M.J., Pope, D.L., Shulman, G.L., Corbetta, M., 2010. Resting interhemispheric functional magnetic resonance imaging connectivity predicts performance after stroke. Ann. Neurol. 67, 365–375.

Chen, X., Lu, B., Yan, C., 2018. Reproducibility of r-fmri metrics on the impact of different strategies for multiple comparison correction and sample sizes. Hum. Brain Mapp. 39, 300–318.

Chen, Y., Tang, S., Wu, W., Kao, H., Kuo, Y., Yang, S., 2017. Alterations of cerebral perfusion in asymptomatic internal carotid artery steno-occlusive disease. Sci. Rep. 7.

Cheng, H.L., Lin, C.J., Soong, B.W., Wang, P.N., Chang, F.C., Wu, Y.T., Chou, K.H., Lin, C.P., Tu, P.C., Lee, I.H., 2012. Impairments in cognitive function and brain connectivity in severe asymptomatic carotid stenosis. Stroke 43, 2567–2573.

Cui, Z., Zhong, S., Xu, P., He, Y., Gong, G., 2013. PANDA: a pipeline toolbox for analyzing brain diffusion images. Front. Hum. Neurosci. 7, 42.

de Weerd, M., Greving, J.P., Hedblad, B., Lorenz, M.W., Mathiesen, E.B., O'Leary, D.H., Rosvall, M., Sitzer, M., de Borst, G.J., Buskens, E., Bots, M.L., 2014. Prediction of asymptomatic carotid artery stenosis in the general population: identification of high-risk groups. Stroke 45, 2366–2371.

Descoteaux, M., Deriche, R., Knosche, T.R., Anwander, A., 2009. Deterministic and probabilistic tractography based on complex fibre orientation distributions. IEEE Trans. Med Imaging 28, 269–286.

Dichgans, M., Leys, D., 2017. Vascular cognitive impairment. Circ. Res. 120, 573–591.

Folstein, M.F., Folstein, S.E., McHugh, P.R., 1975. Mini-mental state". A practical method for grading the cognitive state of patients for the clinician. J. Psychiatr. Res. 12, 189–198.

Grefkes, C., Fink, G.R., 2014. Connectivity-based approaches in stroke and recovery of function. Lancet Neurol. 13, 206–216.

Hartkamp, N.S., Petersen, E.T., Chappell, M.A., Okell, T.W., Uyttenboogaart, M., Zeebregts, C.J., Bokkers, R.P., 2017. Relationship between haemodynamic impairment and collateral blood flow in carotid artery disease. J. Cerebral Blood Flow Metab. 38, 2021–2032.

Hendrikse, J., van Osch, M.J., Rutgers, D.R., Bakker, C.J., Kappelle, L.J., Golay, X., van der Grond, J., 2004. Internal carotid artery occlusion assessed at pulsed arterial spin-labeling perfusion MR imaging at multiple delay times. Radiology 233, 899–904.

Hoptman, M.J., Zuo, X., D'Angelo, D., Mauro, C.J., Butler, P.D., Milham, M.P., Javitt, D.C., 2012. Decreased interhemispheric coordination in schizophrenia: a resting state fMRI study. Schizophr. Res. 141, 1–7.

Hu, Y., Guo, W., Lee, I., Chang, F., Lin, C., Lin, C., Luo, C., Wu, C., Lee, H., 2018. Prolonged cerebral circulation time is more associated with symptomatic carotid stenosis than stenosis degree or collateral circulation. J. Neurointerv. Surg. 10, 476–480.

Huntenburg, J.M., Bazin, P.L., Margulies, D.S., 2018. Large-scale gradients in human cortical organization. Trends Cognit. Sci. 22, 21–31.

Iacoboni, M., Zaidel, E., 2004. Interhemispheric visuo-motor integration in humans: the role of the superior parietal cortex. Neuropsychologia 42, 419–425.

Johnston, J.M., Vaishnavi, S.N., Smyth, M.D., Zhang, D., He, B.J., Zempel, J.M., Shimony, J.S., Snyder, A.Z., Raichle, M.E., 2008. Loss of resting interhemispheric functional connectivity after complete section of the corpus callosum. J. Neurosci. 28, 6453–6458.

Joliot, M., Jobard, G., Naveau, M., Delcroix, N., Petit, L., Zago, L., Crivello, F., Mellet, E., Mazoyer, B., Tzourio-Mazoyer, N., 2015. AICHA: an atlas of intrinsic connectivity of homotopic areas. J. Neurosci. Methods 254, 46–59.

Kelly, C., Zuo, X., Gotimer, K., Cox, C.L., Lynch, L., Brock, D., Imperati, D., Garavan, H., Rotrosen, J., Castellanos, F.X., 2011. Reduced interhemispheric resting state functional connectivity in cocaine addiction. Biol. Psychiatry 69, 684–692.

Layden, E.A., Schertz, K.E., London, S.E., Berman, M.G., 2019. Interhemispheric functional connectivity in the zebra finch brain, absent the corpus callosum in normal ontogeny. Neuroimage 195, 113–127.

Li, J., Gao, L., Xie, K., Zhan, J., Luo, X., Wang, H., Zhang, H., Zhao, J., Zhou, F., Zeng, X., He, L., He, Y., Gong, H., 2017. Detection of functional homotopy in traumatic axonal injury. Eur. Radiol. 27, 325–335.

Lin, C.J., Tu, P.C., Chern, C.M., Hsiao, F.J., Chang, F.C., Cheng, H.L., Tang, C.W., Lee, Y.C., Chen, W.T., Lee, I.H., 2014. Connectivity features for identifying cognitive impairment in presymptomatic carotid stenosis. PLoS ONE 9, e85441.

Margulies, D.S., Ghosh, S.S., Goulas, A., Falkiewicz, M., Huntenburg, J.M., Langs, G., Bezgin, G., Eickhoff, S.B., Castellanos, F.X., Petrides, M., Jefferies, E., Smallwood, J., 2016. Situating the default-mode network along a principal gradient of macroscale cortical organization. Proc. Natl. Acad. Sci. U. S. A. 113, 12574–12579.

Marshall, O., Uh, J., Lurie, D., Lu, H., Milham, M.P., Ge, Y., 2015. The influence of mild carbon dioxide on brain functional homotopy using resting-state fMRI. Hum. Brain Mapp. 36, 3912–3921.

Michels, L., Blok, B.F., Gregorini, F., Kurz, M., Schurch, B., Kessler, T.M., Kollias, S., Mehnert, U., 2015. Supraspinal control of urine storage and micturition in men–an fMRI study. Cerebral Cortex 25, 3369–3380.

Nasreddine, Z.S., Phillips, N.A., Bedirian, V., Charbonneau, S., Whitehead, V., Collin, I., Cummings, J.L., Chertkow, H., 2005. The montreal cognitive assessment, moca: a brief screening tool for mild cognitive impairment. J. Am. Geriatr. Soc. 53, 695–699.

O'Reilly, J.X., Croxson, P.L., Jbabdi, S., Sallet, J., Noonan, M.P., Mars, R.B., Browning, P.G., Wilson, C.R., Mitchell, A.S., Miller, K.L., Rushworth, M.F., Baxter, M.G., 2013. Causal effect of disconnection lesions on interhemispheric functional connectivity in rhesus monkeys. Proc. Natl. Acad. Sci. U. S. A. 110, 13982–13987.

Panczykowski, D.M., Monaco, E.R., Friedlander, R.M., 2014. Connectivity features for identifying cognitive impairment in presymptomatic carotid stenosis. Neurosurgery 74, N9–N11.

Pizoli, C.E., Shah, M.N., Snyder, A.Z., Shimony, J.S., Limbrick, D.D., Raichle, M.E., Schlaggar, B.L., Smyth, M.D., 2011. Resting-state activity in development and maintenance of normal brain function. Proc. Natl. Acad. Sci. U. S. A. 108, 11638–11643.

Power, J.D., Barnes, K.A., Snyder, A.Z., Schlaggar, B.L., Petersen, S.E., 2012. Spurious but systematic correlations in functional connectivity MRI networks arise from subject motion. Neuroimage 59, 2142–2154.

Raichle, M.E., 2015. The brain's default mode network. Annu. Rev. Neurosci. 38, 433–447.

Roland, J.L., Snyder, A.Z., Hacker, C.D., Mitra, A., Shimony, J.S., Limbrick, D.D., Raichle, M.E., Smyth, M.D., Leuthardt, E.C., 2017. On the role of the corpus callosum in interhemispheric functional connectivity in humans. Proc. Natl. Acad. Sci. 114, 13278–13283.

Rosenfield, K., Matsumura, J.S., Chaturvedi, S., Riles, T., Ansel, G.M., Metzger, D.C., Wechsler, L., Jaff, M.R., Gray, W., 2016. Randomized trial of stent versus surgery for asymptomatic carotid stenosis. N. Engl. J. Med. 374, 1011–1020.

Siegel, J.S., Ramsey, L.E., Snyder, A.Z., Metcalf, N.V., Chacko, R.V., Weinberger, K., Baldassarre, A., Hacker, C.D., Shulman, G.L., Corbetta, M., 2016. Disruptions of network connectivity predict impairment in multiple behavioral domains after stroke. Proc. Natl. Acad. Sci. 113, E4367–E4376.

Silvestrini, M., Vernieri, F., Pasqualetti, P., Matteis, M., Passarelli, F., Troisi, E., Caltagirone, C., 2000. Impaired cerebral vasoreactivity and risk of stroke in patients with asymptomatic carotid artery stenosis. JAMA 283, 2122–2127.

Stark, D.E., Margulies, D.S., Shehzad, Z.E., Reiss, P., Kelly, A.C., Uddin, L.Q., Gee, D.G., Roy, A.K., Banich, M.T., Castellanos, F.X., 2008. Regional variation in interhemispheric coordination of intrinsic hemodynamic fluctuations. J. Neurosci. 28, 13754–13764.

Sulter, G., Steen, C., De Keyser, J., 1999. Use of the Barthel index and modified Rankin scale in acute stroke trials. STROKE 30, 1538–1541.

Tyszka, J.M., Kennedy, D.P., Adolphs, R., Paul, L.K., 2011. Intact bilateral resting-state networks in the absence of the corpus callosum. J. Neurosci. 31, 15154–15162.

van Meer, M.P., van der Marel, K., Wang, K., Otte, W.M., El Bouazati, S., Roeling, T.A., Viergever, M.A., van der Sprenkel, J.W.B., Dijkhuizen, R.M., 2010. Recovery of sensorimotor function after experimental stroke correlates with restoration of resting-state interhemispheric functional connectivity. J. Neurosci. 30, 3964–3972.

van Veluw, S.J., Shih, A.Y., Smith, E.E., Chen, C., Schneider, J.A., Wardlaw, J.M., Greenberg, S.M., Biessels, G.J., 2017. Detection, risk factors, and functional consequences of cerebral microinfarcts. Lancet Neurol. 16, 730–740.

Wang, T., Xiao, F., Wu, G., Fang, J., Sun, Z., Feng, H., Zhang, J., Xu, H., 2017. Impairments in brain perfusion, metabolites, functional connectivity, and cognition in severe asymptomatic carotid stenosis patients: an integrated mri study. Neural Plast. 2017, 8738714.

Xing, X.X., Zuo, X.N., 2018. The anatomy of reliability: a must read for future human brain mapping. Sci. Bull. 63, 14–15.

Yan, C., Cheung, B., Kelly, C., Colcombe, S., Craddock, R.C., Di Martino, A., Li, Q., Zuo, X., Castellanos, F.X., Milham, M.P., 2013. A comprehensive assessment of regional

variation in the impact of head micromovements on functional connectomics. Neuroimage 76, 183–201.
Yan, C., Wang, X., Zuo, X., Zang, Y., 2016. DPABI: data processing & analysis for (resting-state) brain imaging. Neuroinformatics 14, 339–351.
Yarkoni, T., Poldrack, R.A., Nichols, T.E., Van Essen, D.C., Wager, T.D., 2011. Large-scale automated synthesis of human functional neuroimaging data. Nat. Methods 8, 665–670.
Yeo, B.T., Krienen, F.M., Sepulcre, J., Sabuncu, M.R., Lashkari, D., Hollinshead, M., Roffman, J.L., Smoller, J.W., Zollei, L., Polimeni, J.R., Fischl, B., Liu, H., Buckner, R.L., 2011. The organization of the human cerebral cortex estimated by intrinsic functional connectivity. J. Neurophysiol. 106, 1125–1165.
Zuo, X., Biswal, B.B., Poldrack, R.A., 2019a. Editorial: reliability and reproducibility in functional connectomics. Front. Neurosci. 13.
Zuo, X.N., Anderson, J.S., Bellec, P., Birn, R.M., Michael, P.M., 2013. An open science resource for establishing reliability and reproducibility in functional connectomics. Sci. Data 1, 140049.
Zuo, X.N., Kelly, C., Di Martino, A., Mennes, M., Margulies, D.S., Bangaru, S., Grzadzinski, R., Evans, A.C., Zang, Y.F., Castellanos, F.X., Milham, M.P., 2010. Growing together and growing apart: regional and sex differences in the lifespan developmental trajectories of functional homotopy. J. Neurosci. 30, 15034–15043.
Zuo, X.N., Xing, X.X., 2014. Test-retest reliabilities of resting-state FMRI measurements in human brain functional connectomics: a systems neuroscience perspective. Neurosci. Biobehav. Rev. 45, 100–118.
Zuo, X.N., Xu, T., Milham, M.P., 2019b. Harnessing reliability for neuroscience research. Nat. Hum. Behav. 3, 768–771.